Comparison of Coarse-Grained Approaches in Predicting Polymer Nanocomposite Phase Behavior

Jason P. Koski,[1] Robert C. Ferrier Jr.,[2] Nadia M. Krook,[3] Huikuan Chao,[2] Russell J. Composto,[3] Amalie L. Frischknecht,[1] and Robert A. Riggleman[2, a)]

[1)]*Sandia National Laboratories, Albuquerque, New Mexico 87185*

[2)]*Department of Chemical and Biomolecular Engineering, University of Pennsylvania, Philadelphia, PA 19104*

[3)]*Department of Materials Science, University of Pennsylvania, Philadelphia, PA 19104*

(Dated: August 9, 2017)

Due to the considerable parameter space, efficient theoretical and simulation methods are required to predict the morphology and guide experiments in polymer nanocomposites (PNCs). Unfortunately, theoretical and simulation methods are restricted in their ability to accurately map to experiments based on necessary approximations and numerical limitations. In this study, we provide direct comparisons of two recently developed coarse-grained approaches for modeling polymer nanocomposites (PNCs): polymer nanocomposite field theory (PNC-FT) and dynamic mean-field theory (DMFT). These methods are uniquely suited to efficiently capture mesoscale phase behavior of PNCs in comparison to other theoretical and simulation frameworks. We demonstrate the ability of both methods to capture macrophase separation and describe the thermodynamics of PNCs. We systematically test how the nanoparticle morphology in PNCs is affected by a uniform probability distribution of grafting sites, common in field-based methods, versus random discrete grafting sites on the nanoparticle surface. We also analyze the accuracy of the mean-field approximation in capturing the phase behavior of PNCs. Moreover, the DMFT method introduces the ability to describe non-equilibrium phase behavior while the PNC-FT method is strictly an equilibrium method. With the DMFT method we are able to show the evolution of non-equilibrium states towards their equilibrium state and a qualitative assessment of the dynamics in these systems. These simulations are compared to experiments consisting of polystyrene grafted gold nanorods in a poly(methyl methacrylate) matrix to ensure the model gives results that qualitatively agree with the experiments. This study reveals that nanoparticles in a relatively high matrix molecular weight are trapped in a non-equilibrium state and demonstrates the utility of the DMFT framework in capturing non-equilibrium phase behavior of PNCs. Both the PNC-FT and DMFT framework are promising methods to describe the thermodynamic and non-equilibrium phase behavior of PNCs.

[a)]Electronic mail: rrig@seas.upenn.edu

I. INTRODUCTION

The inclusion of organic and inorganic nanoparticles into a polymer matrix, commonly referred to as a polymer nanocomposite (PNC), has received widespread interest due to the introduction of enhanced mechanical, electrical, magnetic, and optical properties in polymer-based systems[1]. For example, the spacing between plasmonic nanoparticles, such as gold nanorods (AuNRs), in polymer thin films can be tuned to manipulate the optical properties in these materials[2–5]. It is well-accepted that the particle morphology dictates the resulting material properties of the system, so a key issue in PNCs is an understanding of the fundamental aspects that dictate the distribution of nanoparticles within the polymer matrix. A common strategy to control the distribution of nanoparticles is to graft polymer chains onto the surface of the nanoparticles, since tuning the relative length of the matrix and grafted chains in athermal systems has been shown to affect the spatial arrangement of the nanoparticles[6–9]. However, grafting chains onto the surface of nanoparticles expands the already appreciable parameter space of PNCs with additional factors to consider such as grafting density, enthalpic interactions between the grafts and matrix, and complex grafting architectures.

Processing conditions are also known to play an important role in the final state of the material[10–12]. Often PNCs are spin-coated from solution, after which the solvent rapidly evaporates and vitrifies the matrix polymer, leaving the distribution of nanoparticles in their "as cast" state, which may not be the lowest free energy state[13,14]. Several strategies have been developed to manipulate the final structure of PNCs such as applying shear, external electric or magnetic fields, solvent annealing, and thermal annealing[15–19]. Unfortunately, these approaches are applicable in limited situations and add another step during processing. One such example is the aforementioned AuNRs in polymer thin films where solvent annealing has been shown to affect the structure minimally[14], and thermal annealing will reshape the nanorods into spheres[20], which ruins their attractive optical properties. Electric fields have been used to align AuNRs in solution[21–23] though it is unclear if these strategies translate to AuNRs in a polymer matrix, particularly once the matrix polymer has vitrified. As a result, these AuNR systems are limited to their "as cast" state and it is unclear from experimental characterization alone if these systems are in an equilibrium or non-equilibrium state.

Theory and simulations provide an attractive approach to effectively isolate parameters of interest and reduce the parameter space necessary to consider through experiments. However, theory

and simulations are limited in their ability to accurately replicate experiments due to approximations and numerical limitations that are necessary to make the study of PNCs viable. The majority of our fundamental understanding of PNCs stems from equilibrium models, such as PRISM theory[24–28] and self-consistent field theory (SCFT)[14,29–34]. Nonequilibrium methods remain a particular challenge. Although great progress has been made recently in the systems that can be simulated using atomistic or coarse-grained molecular dynamics, the length and time scales that are tractable still remain somewhat limited. Comprehensive reviews by Ganesan and Jayaraman[35] and by Kumar, Ganesan, and Riggleman[36] discuss theoretical and simulation methods used to study PNCs along with their strengths and limitations in properly modeling these systems. Here, we extend their discussions with two more recent methods, polymer nanocomposite field theory (PNC-FT)[37–39] and dynamic mean-field theory (DMFT),[40,41] where we focus on grafted nanoparticles.

PNC-FT is a field-theoretic simulation approach in which the nanoparticle densities are written as cavity functions that have a strong repulsion with the polymer monomers, and these cavity functions are traced through the particle-to-field transformation to arrive at a model that only depends on chemical potential fields; the theory is a generalization of the hybrid particle-field theory (HPFT) framework developed by Sides and coworkers[42]. As a field-theoretic approach, the PNC-FT is able to circumvent many of the equilibration challenges faced by particle-based simulations of polymer nanocomposites. In more recent years, we extended the original theory of bare particle nanocomposites[37] to grafted particle nanocomposites[38,39]. Unfortunately, the effective use of the grafted nanoparticle theory requires that the grafted polymers are attached to the nanoparticles with a fixed, uniform grafting distribution across the surface of the particles. This uniform grafting distribution is an evenly spaced probability distribution at the surface of the nanoparticle that dictates the location of the grafted chains' first segment. This approximation is often not correct for experimental systems, but relaxing it substantially increases the computational expense of the problem. A further limitation of the PNC-FT method is the difficultly in capturing dynamic and non-equilibrium behavior since the theory is based on equilibrium statistical mechanics. Additionally, field-based models are most efficiently used under a mean-field approximation, commonly referred to as SCFT, where it is assumed that a single field configuration dominates the partition function, thus ignoring fluctuation effects. However, the mean-field approximation can be inaccurate for systems where thermal fluctuations are important and more advanced and computationally expensive numerical schemes are necessary, such as complex Langevin (CL) sampling[43].

Recently, Fredrickson and Orland[40] proposed a dynamic mean-field theory (DMFT) to incorporate polymer chain dynamics into a non-equilibrium partition function via a path integral representation. Shortly after the DMFT framework was proposed, we developed a numerical implementation of this framework to characterize solvent annealing in a block copolymer nanocomposite thin film[41]. This framework is similar to other previously proposed models that implement a particle-to-mesh scheme to interchangeably go between a particle-based model and a field-based model such as self-consistent Brownian dynamics (SCBD)[44], single-chain-in-mean-field (SCMF)[45], and a theoretically informed coarse-grained (TICG) model[46]. As the DMFT approach is based on a non-equilibrium partition function, it has direct access to the dynamic pathways, contrary to the PNC-FT method. Furthermore, implementing discrete grafting, where chains are grafted to specific locations on each nanoparticle, is straightforward in DMFT unlike in PNC-FT. We have also shown that the DMFT framework captures the effect of thermodynamic fluctuations.

In this study, we first compare the effectiveness of the PNC-FT and DMFT approaches in their ability to characterize grafted PNCs. Since these methods are easily constructed from the same thermodynamic model, we can effectively isolate the role of thermal fluctuations and discrete grafting while assessing the numerical efficiencies of each approach. After comparing the PNC-FT and DMFT approaches, we then analyze the non-equilibrium nature of the DMFT. We compare the phase behavior from the DMFT simulations to experiments on polystyrene (PS) grafted gold nanorods (AuNRs) in a poly (methyl methacrylate) (PMMA) matrix. While we do not attempt to exactly reproduce the experimental protocol in our simulations, the experiments provide a basis to assess the trends seen from the DMFT model. The DMFT's access to non-equilibrium states suggests the experiments presented below are in a non-equilibrium state. We emphasize this conclusion is difficult to make with other theoretical or simulation methods or experimental characterization alone. It is worth noting that while the DMFT approach can sample non-equilibrium phenomena, it is currently limited in its ability to accurately map the dynamics of the experimental system. The DMFT framework we present is a Rouse model with Flory interactions and it is unclear how to properly map the relative magnitudes of the nanoparticle and polymer mobility coefficients. Furthermore, in this study we do not consider entanglement effects, though slip link approaches could be implemented to capture these effects[47–51].

The rest of the paper is organized as follows: In the following section, we present details of the experimental methods and characterization. In section III, we provide the key aspects of the PNC-FT and DMFT formalisms used in this study. Section IV describes the numerical methods

used in implementing each model. In section V we discuss the results from the comparison of the PNC-FT and DMFT models along with the corresponding DMFT simulations that are used to compare to the experiments. Finally, we provide a summary and additional discussion in Section VI.

II. EXPERIMENTAL METHODS

All reagents were purchased from Sigma-Aldrich unless otherwise noted. Thiolated polymers were purchased from Polymer Source, Inc.

A. AuNR Synthesis and Functionalization

AuNRs are synthesized as reported elsewhere[2,5,52,53]. AuNRs were functionalized with thiolated polystyrene (PS-SH) with M_n of 11.5 kg/mol. Functionalization proceeds by first preparing a solution containing PS-SH in tetrahydofuran (THF). Next, the as-synthesized AuNRs in water were centrifuged down and the supernatant removed. The concentrated AuNR aliquot was then injected into the THF / PS-SH solution under heavy stirring. The thiolated polymers were allowed to incubate with the AuNRs in THF overnight. Finally, the now functionalized AuNRs were centrifugated and the supernatant was removed and replaced with toluene. The centrifugation and solvent replacement was repeated a total of three times to remove free thiol polymer from solution.

B. Thin Film Preparation

Polymer thin films were prepared by adding 0.7 to 0.4 mg of free poly(methyl methacrylate) (PMMA) (M_n = 1.1 kg/mol or 77 kg/mol) to 100 μL of AuNR solution in toluene. The free PMMA was allowed to dissolve and then 20 μL of the polymer / AuNR solution was spin cast at 2000 RPM onto a silicon wafer for scanning electron microscopy (SEM) imaging. The samples were allowed to dry overnight prior to any imaging.

C. Thin Film Characterization

Thin film PNCs were analyzed by SEM. SEM was performed on a JEOL7500F in low angle backscatter (LABE) mode.

D. SEM Image Analysis

SEM images were analyzed using ImageJ image analysis software (v.1.45S). Prior to analysis of the particle area, images were first thresholded such that the AuNRs were able to be recognized by the software. Then, a macro was run in ImageJ that finds the centers of the AuNRs and calculates the radial distribution function (RDF). The resulting RDF was averaged over 20 images from different locations on the Si wafer of the same sample.

III. MODELING METHODS

A. Model Details

We first present the model for A homopolymers grafted to neutral nanoparticles in a B homopolymer matrix. For notational simplicity, the grafted chains, matrix chains, and nanoparticles will be denoted as G, M, and P, respectively. The polymers are modeled as discrete Gaussian chains with N_G and N_M segments for the grafted and matrix chains, respectively, while the nanoparticles are described by a cavity function with radius R_P. The microscopic density of the polymers is given by

$$\hat{\rho}_K(\mathbf{r}) = \sum_i^{n_K} \sum_j^{N_K} h(\mathbf{r} - \mathbf{r}_{i,j}), \tag{1}$$

where

$$h(\mathbf{r}) = \left(\frac{1}{2\pi a^2}\right)^{d/2} \exp\left(-\frac{\mathbf{r}^2}{2a^2}\right). \tag{2}$$

Here, K is either G or M, n_K is the number of polymer chains of type K, d is the dimensionality of the system, and a is the effective monomer size. The difference between the grafted and matrix chains is that for the grafted chains, one chain end is restricted to the surface of the nanoparticles while there is no such restriction for the matrix chains. The microscopic density of the nanoparticles is given by

$$\hat{\rho}_P(\mathbf{r}) = \sum_i^{n_P} \Gamma(\mathbf{r} - \mathbf{r}_i), \tag{3}$$

where n_P is the number of nanoparticles, and the cavity function $\Gamma(\mathbf{r})$ is defined as

$$\Gamma(\mathbf{r}) = \frac{\rho_0}{2} \operatorname{erfc}\left(\frac{|\mathbf{r}| - \mathrm{R_P}}{\xi}\right). \tag{4}$$

Here, R_P is the radius of the particle and ξ is the length scale in which the particle density goes from ρ_0 inside the core to 0 outside the core.

The polymer chains are connected via a Gaussian bonding potential

$$\beta U_0 = \sum_{i}^{n_K} \sum_{j}^{N_K-1} \frac{3|\mathbf{r}_{i,j} - \mathbf{r}_{i,j+1}|^2}{2b^2}, \tag{5}$$

where b is the statistical segment length of the polymer. Here, we assume that $b_G = b_M = b$. A Helfand compressibility potential[54] is used to enforce an energetic penalty for deviations away from the average system density, ρ_0, given by

$$\beta U_1 = \frac{\kappa}{2\rho_0} \int d\mathbf{r} \, [\hat{\rho}_+(\mathbf{r}) - \rho_0]^2, \tag{6}$$

where $\hat{\rho}_+ = \hat{\rho}_G + \hat{\rho}_M + \hat{\rho}_P$ is the spatially varying total microscopic density and κ controls the strength of the density fluctuations. Finally, a repulsive Flory-like potential is used to include enthalpic repulsions between the grafted and matrix chains

$$\beta U_2 = \frac{\chi}{\rho_0} \int d\mathbf{r} \, \hat{\rho}_G(\mathbf{r}) \hat{\rho}_M(\mathbf{r}), \tag{7}$$

while we treat the nanoparticle cores as enthalpically neutral.

B. Polymer Nanocomposite Field Theory

Here we present the main details of the PNC-FT framework where additional details can be found in our previous works[37–39]. As the PNC-FT framework is a generalization of the HPFT methodology, the derivation of each approach is similar. This section presents a generalized version of the HPFT and PNC-FT frameworks that can leverage the advantages of each model, described further below. The notation "exp" (short for explicit) corresponds with the HPFT approach where the explicit nanoparticle coordinates are retained while "field" corresponds to the PNC-FT framework. Hubbard-Stratonovich transformations are used to decouple the intermolecular interactions and transform the relevant degrees of freedom from particle coordinates to chemical potential fields[55,56]. The result of the particle-to-field transformation is the equilibrium field-theoretic partition function,

$$\mathscr{Z} = z_1 \int d\mathbf{r}^{n_{P,exp}} \int \mathscr{D}w_+ \int \mathscr{D}w_{GM}^{(+)} \int \mathscr{D}w_{GM}^{(-)} \, e^{-\mathscr{H}[\{w\}]}, \tag{8}$$

where z_1 contains the numerical prefactors such as the thermal de Broglie wavelengths and the normalization constants from the Gaussian functional integrals used to de-couple the particle interactions. $\mathscr{H}[\{w\}]$ is the effective Hamiltonian of the system, and $\{w\}$ is the set of chemical

potential fields for our system, $w_+, w_{GM}^{(+)}, w_{GM}^{(-)}$. We note that the explicit nanoparticle coordinates, $\mathbf{r}^{n_{P,exp}}$, remain as degrees of freedom in the partition function while the field-based nanoparticle coordinates are integrated out similar to the polymer coordinates. The effective Hamiltonian is given by

$$\begin{aligned}\mathscr{H}[\mathbf{r}^{n_{P,exp}}, \{w\}] = &\frac{\rho_0}{2\kappa}\int d\mathbf{r}\,[w_+(\mathbf{r})]^2 - i\int d\mathbf{r}\, w_+(\mathbf{r})\,[\rho_0 - \hat{\rho}_{P,exp}(\mathbf{r})] \\ &+\frac{\rho_0}{\chi}\int d\mathbf{r}\,[w_{GM}^{(+)}(\mathbf{r})]^2 + \frac{\rho_0}{\chi}\int d\mathbf{r}\,[w_{GM}^{(-)}(\mathbf{r})]^2 \\ &-n_M \ln Q_M[\mu_M] - n_{P,field}\ln Q_P[\mu_P] \\ &-n_{G,exp}\int d\mathbf{r}\;\sigma_{G,exp}(\mathbf{r})\ln q_{G,exp}[r;\mu_G], \end{aligned} \tag{9}$$

where Q_M, q_G, and Q_P are the partition functions of a single matrix chain, grafted chain, and field-based nanoparticle, respectively. The fields μ_G and μ_M are defined such that they are convolutions of their density function, h, with their conjugated chemical potential fields, w_G and w_M, given by

$$\begin{aligned} w_G &= i[w_+ + w_{GM}^{(+)}] - w_{GM}^{(-)}, \\ w_M &= i[w_+ + w_{GM}^{(+)}] + w_{GM}^{(-)}. \end{aligned} \tag{10}$$

The field μ_P takes the form[38]

$$\mu_P(\mathbf{r}) = (\Gamma * iw_+)(\mathbf{r}) - n_{G,field}\left(\sigma_{G,field} * \ln q_{G,field}\right)(\mathbf{r}), \tag{11}$$

where the asterisk indicates a convolution operation. The first term in Eq. 11 encompasses the interactions experienced by the nanoparticle core while the second term represents the free energy of a grafted chain terminating at the surface of the nanoparticle. Without the second term, the nanoparticle distribution would be unaffected by the grafted chains. The normalized grafting site distributions, σ_G, are defined through a convolution of a grafting function with the nanoparticle centers and divided by the number of nanoparticles. The uniform grafting function is defined by

$$\Gamma_{\sigma,uniform}(\mathbf{r}) = \frac{1}{\sigma_0}\,\exp\left[-\left(\frac{3(|\mathbf{r}| - R_P - \xi)}{2b^2}\right)^2\right], \tag{12}$$

where σ_0 is defined to enforce $\int d\mathbf{r}\,\Gamma_\sigma(\mathbf{r}) = 1$. In this study, when using the PNC-FT framework we only ever use discrete grafting when we have no field-based particles and a single explicit particle that is fixed in the center of the box. Discrete grafting with field-based particles requires a discretization of the unit-sphere to properly account for the rotational degrees of freedom of the asymmetric particles and significantly increases the computational expense of the problem[37,39].

This problem is further exacerbated for numerous discrete grafted particles because each uniquely grafted particle requires a sampling of the discretized unit-sphere. However, these problems do not arise for a single fixed particle. The discrete grafting function for a particle fixed in the center of the box is defined as

$$\Gamma_{\sigma,discrete}(\mathbf{r}) = \frac{1}{\sigma_0}\sum_{i}^{n_G}\exp\left[-\left(\frac{3(|\mathbf{r}-\mathbf{r}_C|-[(R_P+\xi)\cdot\mathbf{u}_i])}{2b^2}\right)^2\right], \tag{13}$$

where $\mathbf{r}_C$ is the center of the box and $\mathbf{u}_i$ is a randomly determined orientation vector of magnitude 1. We note that the grafting distributions defined here represent the distribution of the first grafted segment of the grafted chains in a field-theory context.

The HPFT formalism is realized by setting $n_{P,field} = 0$ while the pure field-based PNC-FT formalism is realized by setting $n_{P,exp} = 0$. The explicit particles allow for exact control and knowledge of a particle's position while the field-based particles lead to rapid calculations of the probability distribution of several particles. The combination of both these approaches allows for efficient calculation of the particle distribution around a single explicit particle, which can be used to calculate the radial distribution function (RDF), g(r). In this study, we only ever set $n_{P,exp} = 0$ or $n_{P,exp} = 1$ where the single explicit particle is fixed in the center of the box.

C. Dynamic Mean Field Theory

Here we present the main details of the DMFT framework where additional details can be found in our previous work[41]. The model is developed by writing an overdamped Langevin equation of motion for the monomers where we neglect hydrodynamic interactions,

$$\frac{d\mathbf{r}_{k,s}}{dt} = D\beta\left[\mathbf{f}^{b}_{k,s}(t)+\mathbf{f}^{nb}_{k,s}(t)\right]+\Theta_{k,s}(t). \tag{14}$$

Here, $\mathbf{r}_{k,s}$ is the position of monomer s on the k^{th} chain, D is the monomeric diffusion coefficient, $\mathbf{f}^{b}_{k,s}$ is the bonded force, $\mathbf{f}^{nb}_{k,s}$ is the nonbonded force, and $\Theta_{k,s}(t)$ is the Gaussian white noise that satisfies

$$\left\langle\Theta_{k,s}(t)\right\rangle = 0, \tag{15}$$

$$\left\langle\Theta_{k,s}(t)\Theta_{k',s'}(t')\right\rangle = 2D\beta\,\delta_{k,k'}\delta_{s,s'}\delta_{t,t'}. \tag{16}$$

The polymers are modeled as discrete Gaussian chains with the bonding potential described by Eq. 5. This leads to a bonding force $\mathbf{f}^{b}_{k,s} = (-3/b^2)[(\mathbf{r}_{k,s}-\mathbf{r}_{k,s-1})+(\mathbf{r}_{k,s}-\mathbf{r}_{k,s+1})]$ where the first

term is neglected for the first segment and the second term is neglected for the last segment of each chain, and the t dependence on $\mathbf{r}$ is suppressed for clarity. In regards to the grafted chains, because we have direct access to the explicit particle coordinates in a DMFT simulation, we simply generate random points on the surface of the nanoparticles to act as the grafting sites for the grafted chains. Specifically, we fix n_G/n_P grafting sites for each particle at a distance $R_P + \xi$ from the center of the particle. These grafting sites do not contribute to the potentials defined in Eqs. 6 and 7. The first grafted polymer monomer interacts with the grafting site via a Gaussian bond such that its distribution matches Eq. 13. Each nanoparticle has a unique grafting distribution. The non-bonded forces $\mathbf{f}^{(\mathrm{nb})}(\mathbf{r},t)$ are given as the convolution between the gradient of the non-bonded potential, $-\nabla u(\mathbf{r})$, and the microscopic density $\hat{\rho}(\mathbf{r},t)$ with the form

$$\mathbf{f}^{(\mathrm{nb})}(\mathbf{r},t) = -\int d\mathbf{r}'\, \nabla u(\mathbf{r}-\mathbf{r}')\,\hat{\rho}(\mathbf{r}',t). \tag{17}$$

Previous works[37,57] have shown that the form of u is a convolution of the density functions of each component (h for the polymers and Γ for the nanoparticles). For example, the non-bonded potential of the Helfand compressibility potential defined in Eq. 6 between a polymer and nanoparticle is given by $u(\mathbf{r}-\mathbf{r}') = \frac{\kappa}{2\rho_0}\int d\mathbf{r}'' h(\mathbf{r}''-\mathbf{r})\Gamma(\mathbf{r}''-\mathbf{r}')$.

A Martin-Siggia-Rose (MSR) functional integral is then used to represent all possible configurations in space and time in a dynamic partition function where the dynamics obey the equation of motion, Eq. 14. The dynamic partition function is given by

$$\mathscr{Z} = \prod_t \prod_{k,s} \int d\mathbf{r}_{k,s}(t) \left\langle \delta\left[\mathbf{r}_{k,s}(t+\Delta t) - \mathbf{r}_{k,s}(t) - D\beta\Delta t(\mathbf{f}^b_{k,s}(t) + \mathbf{f}^{nb}_{k,s}(t)) - \eta_{k,s}(t)\right]\right\rangle. \tag{18}$$

Here, η is the stochastic process integrated over a single time step of size Δt. The integrals in Eq. 18 sum over all possible trajectories of the monomers, while the delta function selects only those that follow a discretized form of Eq. 14, and the average is over all realizations of the noise, $\eta_{k,s}(t)$. Next, the identity

$$\begin{aligned} 1 &= \int \mathscr{D}\rho\, \delta[\rho - \hat{\rho}] \\ &= \int \mathscr{D}\rho \int \mathscr{D}\phi\, e^{i\Delta t \sum_t \int d\mathbf{r}\, \phi(\mathbf{r},t)[\rho(\mathbf{r},t) - \hat{\rho}(\mathbf{r},t)]}, \end{aligned} \tag{19}$$

is used to introduce the continuous density field, $\rho(\mathbf{r},t)$ and the conjugate response field $\phi(\mathbf{r},t)$ that arises from the exponential representation of the delta functional in going from the first to the second line in Eq. 19. Eq. 19 allows us to replace the microscopic density, $\hat{\rho}(\mathbf{r},t)$ with the continuous density field $\rho(\mathbf{r},t)$ in the nonbonded force term. After some manipulation, the dynamic

partition function can be written as

$$\mathscr{Z} = \int \mathscr{D}\phi \int \mathscr{D}\rho e^{A}, \tag{20}$$

$$A = i\Delta t \sum_{t} \int d\mathbf{r}\phi(\mathbf{r},t)\rho(\mathbf{r},t) + n\log Q[\rho,\phi], \tag{21}$$

where Q is the dynamic single-chain partition function and its form is given in Fredrickson and Orland[40]. Next, we follow previous work[40,41] by implementing a dynamic mean-field approximation. We can then solve the mean-field representation of the dynamic partition function by

$$\frac{\delta A}{\delta \phi} = \frac{\delta A}{\delta \rho} = 0, \tag{22}$$

which leads to

$$\phi(\mathbf{r},t) = 0, \tag{23}$$

$$\rho(\mathbf{r},t) = \langle \hat{\rho}(\mathbf{r},t) \rangle . \tag{24}$$

Since $\phi(\mathbf{r},t) = 0$ the dynamics can be evolved according to single-chain dynamics where a single chain interacts in a continuous density field, $\rho(\mathbf{r},t)$. Here, it is important to note that Eq. 14 can be used to evolve the polymer chain dynamics where the continuous density field, $\rho(\mathbf{r},t)$, is replaced with the microscopic density in the nonbonded interactions such that $\mathbf{f}^{nb}(\mathbf{r},t) = -\int d\mathbf{r}' \nabla u(\mathbf{r} - \mathbf{r}')\rho(\mathbf{r}',t)$. This result allows us to efficiently evaluate the non-bonded forces, invoke the same potentials defined in Eqs. 6 and 7, and allow for the same potentials to be used in both PNC-FT and the DMFT framework.

IV. NUMERICAL METHODS

A. Polymer Nanocomposite Field Theory

Complex Langevin sampling is used to sample the complex fields appearing in the partition function and corresponding Hamiltonian (*e.g.* Eqs. 8 and 9)

$$\left(\frac{\partial w(\mathbf{r})}{\partial t}\right) = -\lambda \left(\frac{\delta \mathscr{H}}{\delta w(\mathbf{r})}\right) + \eta(\mathbf{r},t) \tag{25}$$

where t is a fictitious time, λ is the step size of the field evolution, and $\eta(\mathbf{r},t)$ is a Gaussian white noise term that obeys the statistics

$$\langle \eta(\mathbf{r},t) \rangle = 0 \tag{26}$$

$$\langle \eta(\mathbf{r},t)\eta(\mathbf{r}',t') \rangle = 2\lambda\delta(\mathbf{r}-\mathbf{r}')\delta(t-t'). \tag{27}$$

We note that in the absence of the noise term ($\eta(\mathbf{r},t)=0$), Eq. 25 drives the system towards the mean-field (SCFT) solution. A first-order semi-implicit operator splitting technique[58] is used to discretize Eqn. 25 in our implementation.

B. Dynamic Mean-Field Theory

The numerical scheme used here to implement the DMFT framework closely follows our previous work[41]. Here, we briefly recap the key ingredients. In this scheme, instead of the Euler-Maruyama discretization shown in Eq. 18, we adopt another numerical discretization of the Langevin equation of motion for the polymer segments proposed by Grønbech-Jensen and Farago (GJF)[59] to achieve stable trajectories and accurate thermodynamic properties. For a given polymer segment (k,s) under the GJF form, its position is updated as

$$\begin{aligned}\mathbf{r}_{k,s}(t_n) = 2\,b_t\,\mathbf{r}_{k,s}(t_{n-1}) - a_t\,\mathbf{r}_{k,s}(t_{n-2}) + b_t\,\delta t^2[\mathbf{f}^{(\mathrm{b})}_{k,s}(t_{n-1}) + \mathbf{f}^{(\mathrm{nb})}_{k,s}(t_{n-1})] \\ + \frac{b_t\,\delta t}{2}[\theta_{k,s}(t_n) + \theta_{k,s}(t_{n-1})],\end{aligned} \tag{28}$$

where δt is the time step and a_t and b_t are two integration parameters defined by

$$a_t = \frac{1-\frac{\delta t}{2D\beta m_{k,s}}}{1+\frac{\delta t}{2D\beta m_{k,s}}}, \tag{29}$$

$$b_t = \frac{1}{m_{k,s}+\frac{\delta t}{2D\beta}}, \tag{30}$$

where $m_{k,s}$ is the mass of segment (k,s), respectively. The Gaussian random variable $\theta_{k,s}(t_n)$ used in the above equations has the following statistics

$$< \theta_{k,s}(t_n) > = 0, \tag{31}$$

$$< \theta_{k,s}(t_n)\theta_{k',s'}(t_{n'}) > = \frac{2\delta t}{D\beta}\delta_{n,n'}\delta_{k,k'}\delta_{s,s'}. \tag{32}$$

Under the DMFT framework the bonded forces arise directly from the molecular configurations, while the non-bonded forces, $\mathbf{f}^{(\mathrm{nb})}_{k,s}(t)$ are calculated from a continuous density field $\rho(\mathbf{r},t)$. To evaluate the field, a first-order particle-to-mesh (PM) technique[60,61] is implemented upon a collection of molecules with explicit particle coordinates $\hat{\rho}(\mathbf{r},t)$ evolved according to the GJF scheme. Then, the non-bonded forces $\mathbf{f}^{(\mathrm{nb})}(\mathbf{r},t)$ are evaluated using $\mathbf{f}^{nb}(\mathbf{r},t) = -\int d\mathbf{r}'\nabla u(\mathbf{r}-\mathbf{r}')\rho(\mathbf{r}',t)$. Finally, $\mathbf{f}^{(\mathrm{nb})}(\mathbf{r},t)$ is mapped from the values on the mesh-grind to the segment (k,s) by using the PM technique again, which gives the non-bonded forces on the segment, $\mathbf{f}^{(\mathrm{nb})}_{k,s}(t)$.

The nanoparticles experience torque from the grafting of polymers to the fixed sites on the nanoparticle surface, which requires evolution of the rotational dynamics. To address this requirement in a concise way, we use Brownian dynamics of the rotational angle $\psi_i(t)$ to describe the rotational dynamics of the i^{th} nanoparticle rotating about the axis running through the nanoparticle center and vertically aligned with the 2D simulation plane. The $\psi_i(t)$'s equation of motion is given as

$$\psi_i(t_n) = \psi_i(t_{n-1}) + \mu_r \mathbf{T}_i(t_{n-1})\delta t + \theta_i^r(t_n), \tag{33}$$

where μ_r is the rotational mobility that is inversely proportional to the nanoparticle moment of inertia, $V_P \rho_o R_P^2$, where V_P is the volume of the nanoparticle and $\theta_i^r(t_n)$ is Gaussian white noise with statistics

$$< \theta_i^r(t_n) > = \mathbf{0}, \tag{34}$$

$$< \theta_i^r(t_n)\theta_j^r(t_{n'}) > = 2\mu_r \delta t \delta_{n,n'} \delta_{i,j}. \tag{35}$$

The torque applied on the i^{th} nanoparticle, $\mathbf{T}^i(t_n)$, directly comes from the harmonic bonding between the grafted chain-ends and the graft sites on the nanoparticle surface and has the form

$$\mathbf{T}_i(t_n) = \frac{3}{b^2} \sum_k^{N_G} [\mathbf{r}_{g,k}^i(t_n) - \mathbf{r}_{i,c}(t_n)] \times [\mathbf{r}_k(0,t_n) - \mathbf{r}_{g,k}^i(t_n)], \tag{36}$$

where $\mathbf{r}_k(0,t_n)$ is the position of the zeroth segment in the k^{th} grafted chain harmonically bonded to the k^{th} graft site, $\mathbf{r}_{g,k}^i(t_n)$, fixed on the surface of the i^{th} nanoparticle whose center is located at the position, $\mathbf{r}_{i,c}(t_n)$.

C. Numerical Parameters

All calculations are conducted in 2D to most efficiently compare each model. Thus, the grafted nanoparticles are confined to only move in 2D. In all calculations, $b = 1.0$, $a = \xi = (1/3)b$, and $\kappa = 5$. The remaining parameters are varied depending on the context of the problem and mentioned explicitly at the beginning of the corresponding Results section below. A key parameter is the dimensionless chain density, C, defined as $C = n_M R g^d / V$, where d is the dimensionality of the problem and V is the volume of the system. Here, Rg is the unperturbed radius of gyration given by $b\sqrt{(N-1)/6}$. As C is lowered, the role of thermal fluctuations increases such that the mean-field approximation becomes increasingly invalid.

In the PNC-FT calculations, the quantity $\Delta t\lambda$ that shows up after Eq. 25 is discretized is set to 10^{-5} for the w_+ field and 10^{-6} for the w_{AB} fields. Though larger timesteps are possible to equilibrate the systems faster, they are not necessary due to overall efficiency of the simulations. In the CL simulations, approximately 50,000 steps were necessary to equilibrate the system. After the system was equilibrated, the systems were run for over an additional 2 million steps to calculate the average density fields, which were sampled every 200 steps. The SCFT solution was determined when the quantity $\Delta H/V \leq 10^{-9}$, where ΔH is the difference in the Hamiltonian after 200 steps.

For all DMFT simulations, the mass of the polymer segments is set to 1 while for nanoparticles the mass is set as the volume $V_P = \rho_0 \pi R_P^2$. The diffusion coefficients of the polymers are set to 1 while the nanoparticle diffusion coefficient is set to $(V_P\rho_0)^{-1}$. The DMFT timestep $\delta t = 0.04$ such that for example, 2500 DMFT steps equates to $t = 100$. Unlike the PNC-FT calculations, assessing equilibration of the DMFT simulations is non-trivial. As a result, depending on the system we calculate the density profile, brush profiles, or RDF of the nanoparticles over every $\Delta t = 40,000$ to analyze the evolution of the nanoparticle structure. This is described in additional detail in the corresponding Results sections.

In the DMFT simulations used to compare with the experiments, we use C of the experimental system to map our simulation parameters. Specifically, we choose a statistical segment of a polymer $b = 1$ and a total system density $\rho_0 = 3.615$. From mapping the experimental unperturbed radius of gyration to the model, $b \approx 1.47$ nm and each coarse-grained monomer has an approximate molecular weight of 0.5 kg/mol. We assume that the statistical segment size of PS is equal to the statistical segment size of PMMA. The radius of the particle, R_P, was chosen to be $4.073b$ (6 nm) and $N_G = 23$ (11.5 kg/mol) to match the experimental system. Previous calculations have shown that grafting densities of 1.0 chains$/b^2$ in 3D gives grafted polymer density profiles equal to 1.0 chains$/b$ in 2D[62]. As a result, mapping the experimental grafting density, $\sigma = 0.28$ chains/nm^2, to the theory leads to $\sigma = 0.6075$ chains/b. Here, we use experimental reference value $\chi = 0.04$[63] based on a reference volume of approximately 0.16 nm^3. After accounting for our reference volume, ρ_0^{-1}, we map χN_M from the experimental system to the model such that χ is set to 0.2 in all non-athermal calculations.

V. RESULTS

A. Macro Phase Behavior and Approximation Validity

We first assess the macrophase separation of an enthalpic PNC system using a SCFT PNC-FT calculation, CL PNC-FT simulations, and DMFT simulations, which for brevity we will shorthand as SCFT, CL, and DMFT, respectively. Our first goal is to assess both the mean-field approximation and the influence of discrete grafting sites on the thermodynamics of our system. The SCFT calculation uses a mean-field approximation while the CL and DMFT methods include thermal fluctuations. In both the SCFT and CL methods, we assume uniform grafting on the nanoparticle surfaces, while the DMFT simulations use discrete grafting sites. We note that discrete grafting is more representative of experiments and it is therefore useful to understand where the uniform grafting approximation breaks down. In these calculations, $C = 3.2$, $N_M = 60$, $N_G = 20$, and $\chi = 0.2$. We use 50 nanoparticles of size $R_P = 2.5b$ in a $21.6b$ x $252b$ box with 45 x 525 grid points. In all calculations, we start with the grafted nanoparticles located in the center of the box. As a result, the DMFT simulations equilibrate quickly such that the nanoparticle structure stops changing after the first $\Delta t = 40,000$ window. This holds true for all results presented in this section. To ensure ample equilibration, all DMFT simulations in this section were run for $t = 400,000$.

Figure 1 shows the grafted nanoparticle volume fraction (nanoparticles plus grafts) ϕ_{P+G} for each model using two grafting densities, $\sigma = 0.1$ chains/b and $\sigma = 1.0$ chains/b that equate to 2 and 16 grafted chains per particle, respectively. In each condition, there is distinct macrophase separation. For the low grafting density, the grafted nanoparticle distribution from the uniform grafting approximation does not agree with the discrete grafting of the DMFT method. However, the grafted nanoparticle distribution in all three methods agree very well at the high graft density though there is a larger gradient in the grafted nanoparticle distribution with the CL and DMFT methods due to the inclusion of fluctuations. At the lower grafting density $\sigma = 0.1$ chains/b, the SCFT and CL methods predict the polymer-rich phase to contain $\phi_{P+G} \approx 0.04$ and the grafted particle-rich phase to contain $\phi_{P+G} \approx 0.65$ while the DMFT method predicts the polymer and grafted particle-rich phases to be strongly phase separated with $\phi_{P+G} = 0$ and $\phi_{P+G} = 1.0$, respectively. When $\sigma = 1.0$ chains/b, each model predicts strong macrophase separation in each case with $\phi_{P+G} = 0$ and $\phi_{P+G} = 1.0$ in the polymer and particle-rich phases, respectively. As mentioned previously, the difference in the CL and DMFT methods is the use of uniform vs. discrete grafting.

When the grafting density is low, this approximation greatly affects the macrophase behavior of the system.

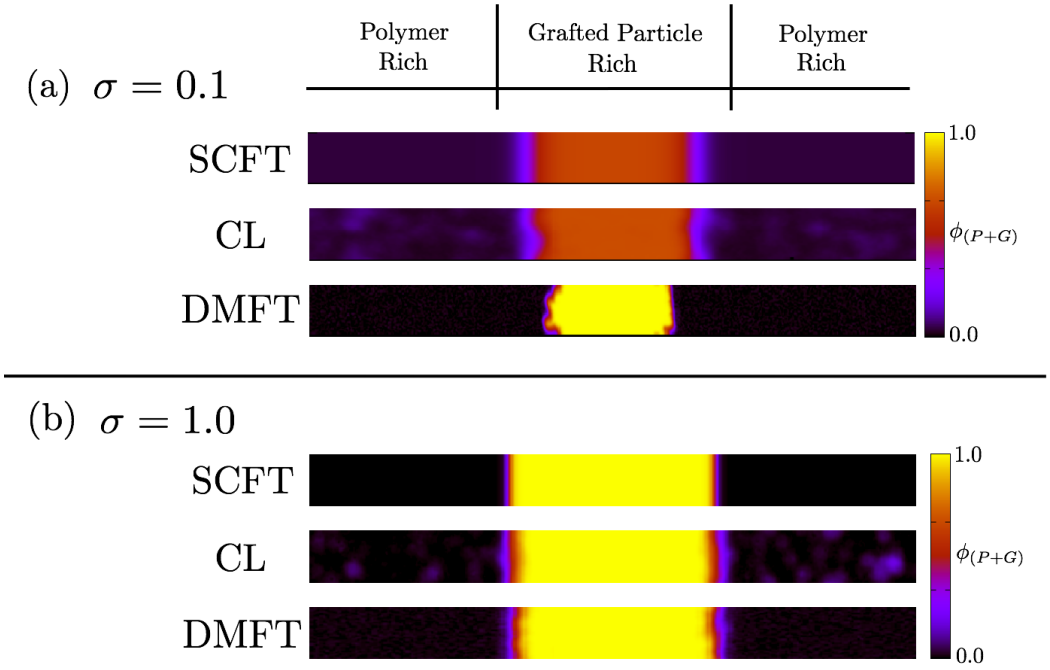

Figure 1. Grafted nanoparticle volume fraction of an enthalpic PNC system using a SCFT calculation, CL simulations, and DMFT simulations for (a) $\sigma = 0.1$ chains/b (2 grafted chains per particle) and (b) σ = 1.0 chains/b (16 grafted chains per particle). The columns are used to emphasize the corresponding polymer- and grafted nanoparticle-rich phases. Each system contains 50 nanoparticles of size $R_P = 2.5b$ with $C = 3.2$, $N_M = 60$, $N_G = 20$, and $\chi = 0.2$. The CL and DMFT simulations are averaged over 3 independent trajectories.

To investigate the role of these approximations, we analyze the details of the particle packing by calculating the RDF, $g(r)$, in each model. Figure 2 shows the RDF using the SCFT, CL, and DMFT models with the same parameters as in Figure 1 except that we include $\sigma = 0.5$ chains/b and are now using 20 particles in a $60b$ by $60b$ box with 125 grid points in each direction. Moreover, to calculate the RDF in the SCFT and CL methods, we place a single explicit particle that is fixed in the center of the box and calculate $g(r)$ based on the distribution of field-based particles around the explicit particle.

The packing of the nanoparticles is increasingly sensitive to the treatment of the grafting sites as the grafting density is decreased. For the lowest grafting density, in Figure 2a we see that the CL and SCFT curves significantly differ from the DMFT curve. Notably, using the DMFT method

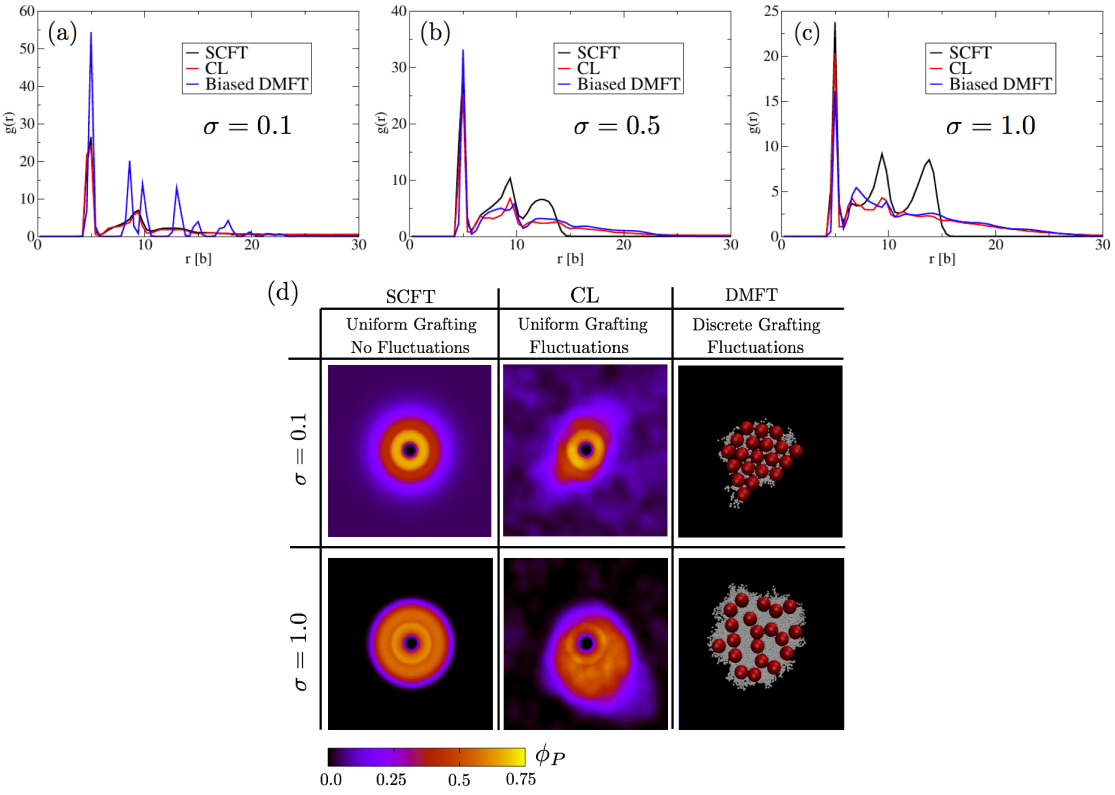

Figure 2. RDF of an enthalpic PNC system using a SCFT calculation, CL simulations, and DMFT simulations for (a) $\sigma = 0.1$ chains/b (2 grafted chains per particle), (b) $\sigma = 0.5$ chains/b (8 grafted chains per particle), and (c) σ = 1.0 chains/b (16 grafted chains per particle). Each system contains 20 nanoparticles of size $R_P = 2.5b$ with $C = 3.2$, $N_M = 60$, $N_G = 20$, and $\chi = 0.2$. The CL simulations are averaged over 10 independent trajectories while the DMFT simulations are averaged over 3 independent trajectories. (d) Visualization of a SCFT calculation, CL simulations, and DMFT simulations displaying the nanoparticle volume fraction for $\sigma = 0.1$ chains/b and $\sigma = 1.0$ chains/b.

for $\sigma = 0.1$ chains/b, we observe several discrete peaks in the RDF that represent close packing of nanoparticles around a central particle, which is much less prominent in the SCFT and CL methods. Due to the discrete grafting of the DMFT model, the particles can rotate and rearrange more easily into a hexagonal lattice structure to minimize the unfavorable $A - B$ contacts. As the grafting density increases, we see that the CL curve agrees with the DMFT curve, though the lack of fluctuations in the SCFT method still leads to notable discrepancies with the other two curves. Here, the SCFT curve displays refined peaks indicating perfect, angularly smooth solvation shells around a central particle (Figure 2d). However, both the CL and DMFT models indicate that fluctuations affect the packing of the particles in the aggregate leading to RDFs that are both lower

in magnitude and extend out to greater distances than the SCFT RDF. Nevertheless, each method still predicts macrophase separation, and in this strong segregation limit the concentrations in the phases were predicted to be approximately equal using all three methods.

To further explore the comparison of the methods' ability to capture PNC-FT phase behavior, we calculate RDFs for athermal systems ($\chi = 0$) across varying N_G and σ values as shown in Figure 3. We hold $N_M = 60$ constant. In athermal PNCs, we expect the particles to be dispersed at low values of N_M/N_G (≈ 2) and phase separated at high values of N_M/N_G (≈ 5) due to entropic dewetting of the grafted polymers by the matrix polymers, although the location of the phase boundary also depends on grafting density and particle size[6–9,33] . While in most cases the inclusion of fluctuations in the PNC-FT method via CL improves the comparison to the DMFT method, we see that at high σ and high N_G, all three curves show good agreement in their RDFs. In these conditions, while the nanoparticles show some preferred clustering at short distances, the nanoparticles are overall dispersed at larger distances. Therefore, the effect of fluctuations is not important when the nanoparticles are prominently dispersed and far away from conditions that promote macrophase separation. However, we see that for $\sigma = 0.5$ chains/b and $N_G = 60$ that the SCFT curve has a much less pronounced peak than the other two curves. This result indicates that the inclusion of fluctuations in conditions that are closer to macrophase separation alters the overall phase behavior. Furthermore, as we saw in Figure 2, fluctuations are important when the nanoparticles are forming prominent aggregates in that they alter the packing of the nanoparticles.

Similar to Figure 2, as the grafting density is increased, we see an increasing agreement between the CL and DMFT curves. However, we see that when $N_G = 60$, the CL and DMFT curves agree at $\sigma = 0.5$ chains/b while at $N_G = 20$, the curves only agree when $\sigma = 1.0$ chains/b. At $N_G = 6$, there are prominent discrepancies between the CL and DMFT curves even at $\sigma = 1.0$ chains/b. These results show that the validity of the uniform grafting approximation is not solely dependent on the grafting density, but on both the grafting density and the grafted chain length. As the grafted chain length is increased, the discrete grafting of the chains matters less because the brush profile of the grafted chains is less affected by the specific grafting sites as the chains are more able to wrap around the surface of the particle.

Figure 4 provides visualizations to support that the uniform grafting approximation is more accurate with both high grafting density and grafted chain length. Specifically, we show the brush profiles of a single, explicit particle using a SCFT calculation with uniform grafting, a SCFT calculation with discrete grafting, and DMFT simulations for $\sigma = 0.1$ chain/b and $\sigma = 1.0$ chains/b

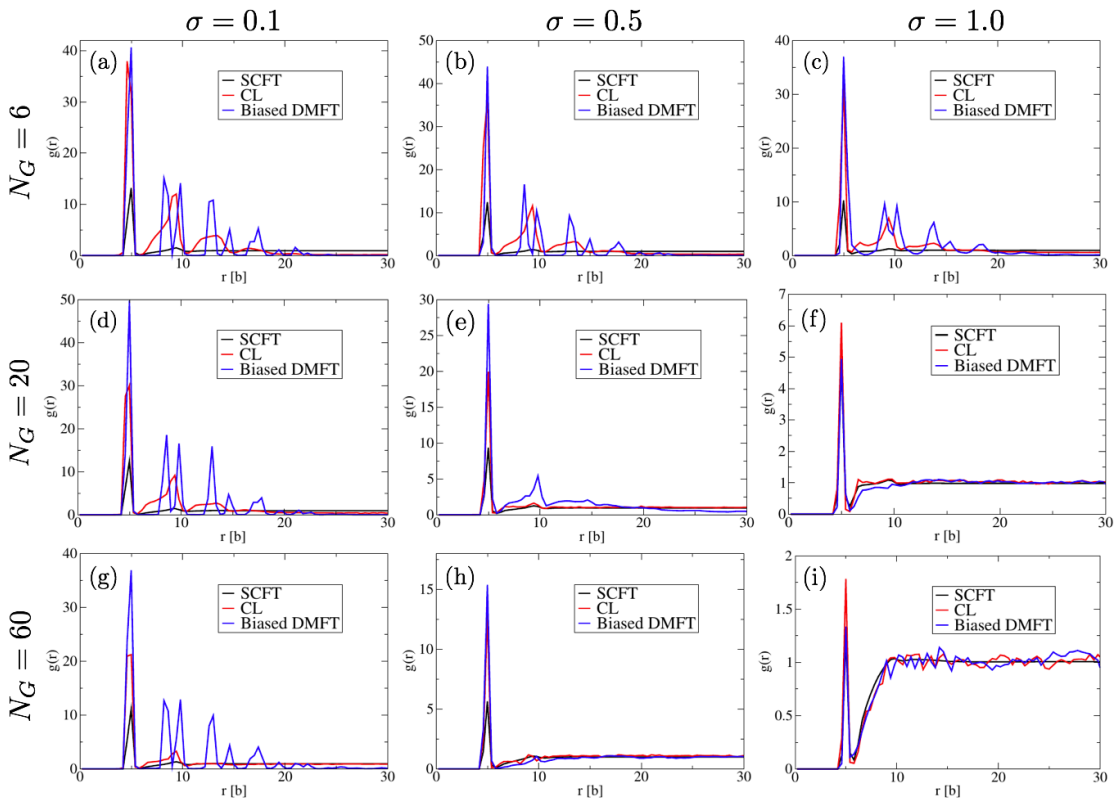

Figure 3. RDF of an athermal PNC system ($\chi = 0$) using a SCFT calculation, CL simulations, and DMFT simulations for (a,d,g) $\sigma = 0.1$ chains/b (2 grafted chains per particle), (b,e,h) $\sigma = 0.5$ chains/b (8 grafted chains per particle), and (c,f,i) σ = 1.0 chains/b (16 grafted chains per particle). The grafted chain length is varied such that (a-c) N_G = 6, (d-f) $N_G = 20$, and (g-i) N_G = 60. Each system contains 20 nanoparticles of size $R_P = 2.5b$ with $C = 3.2$ and $N_M = 60$. The CL simulations are averaged over 10 independent trajectories while the DMFT simulations are averaged over 3 independent trajectories.

each with $N_G = 6$ and $N_G = 60$. In analyzing the visualizations from these calculations, it is clear that the discrepancy in the profiles of the grafted chains is greatest when both the grafting density and grafted chain length are small; the agreement among the methods improves as each of these values increases. We note that treating a many-particle SCFT or CL simulation would require integrating over all possible nanoparticle orientations, which renders the calculations significantly more expensive[39].

In summary, the uniform grafting approximation breaks down as both the grafting density and grafted chain length decrease. Thermal fluctuations play a prominent role in the macro PNC phase behavior when the system is close to the phase separated-dispersion phase boundary. Furthermore, thermal fluctuations affect the packing of particles that are aggregated in that they reduce the order

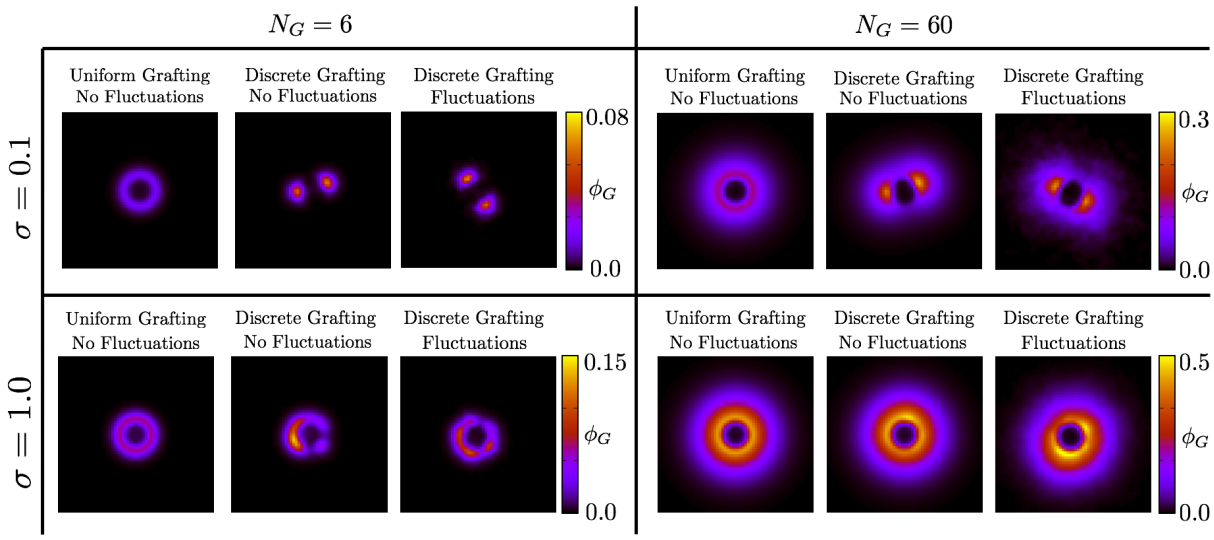

Figure 4. Brush profile comparison of grafted chains to a single fixed particle with varying σ and N_G. In each case, $C = 3.2$, $N_M = 60$, and $\chi = 0$. Each σ and N_G displays calculations with uniform grafting and no fluctuations, discrete grafting and no fluctuations, as well as discrete grafting and fluctuations. The units of σ are in chains/b. In the discrete grafting conditions, different grafting sites are used in each case. The colorbar denotes the volume fraction of the grafted chains.

of the packing.

B. Random vs. Biased DMFT Initialization

We next investigate the kinetics of phase separation and self-assembly in the DMFT approach and their dependence on the initialization of the system. In all cases, we run 3 trajectories for $t = 1,000,000$ with 20 nanoparticles of $R_P = 4.073b$ in a $186.4b$ by $186.4b$ box and 315 grid points to a side. This equates to a nanoparticle volume fraction of $\phi_P \approx 0.03$. In this section, $\rho_0 = 3.615$, $N_G = 23$, $\sigma = 0.6075$ chains$/b$, and $\chi = 0.2$ in all cases. Figure 5 shows the RDFs for the three matrix molecular weights ($N_M = \{4, 23, 154\}$) where in each condition, the nanoparticles are initially either randomized or biased as a single cluster in the center of the box. As the matrix molecular weight increases, the RDF peaks increase. When the nanoparticles are biased and put into the N_M = 23 and N_M = 154 conditions, the RDF shows that the DMFT framework predicts the system will macrophase separate. For N_M = 4, whether the particles are randomized or biased, the nanoparticles end up dispersed in the polymer matrix. However, the DMFT simulations show that the initialization protocol leads to long-time changes in the RDF for N_M = 23 and N_M = 154.

While the biased simulations remain as a single aggregate throughout the simulation, the random simulations coarsen into larger and larger clusters but never form a single macrophase separated aggregate due to the increased time it takes for larger clusters to run into one another. This point is described further below in conjunction with Figure 7. The biased simulations remaining as a single aggregate suggest that macrophase separation is the equilibrium state, which is expected due to the high χN_M values for $N_M = 23$ and $N_M = 154$.

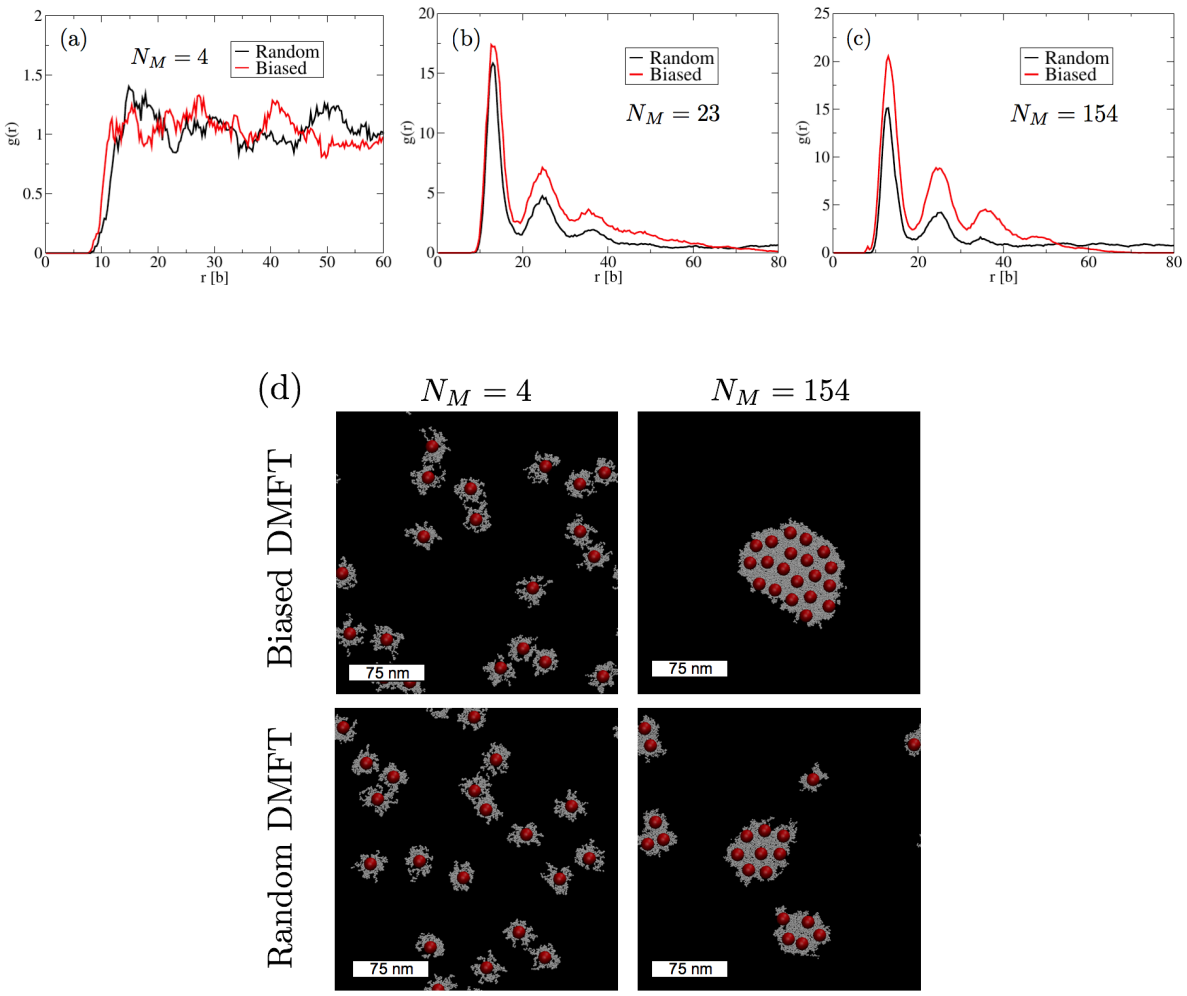

Figure 5. Comparison of RDF from DMFT simulations with random (black) and biased (red) initial conditions for $N_M = 4$ (a), $N_M = 23$ (b), and $N_M = 154$ (c). The RDFs are calculated from t = 960,000 to 1,000,000. Visual representations are presented below for the random and biased DMFT simulations each with $N_M = 4$ and $N_M = 154$ at t = 1,000,000. Each condition is averaged over 3 trajectories.

A significant result from these simulations is shown in Figure 6. Figure 6 shows the RDF for $N_M = 4$ and $N_M = 154$ with random and biased initial conditions at different times during the

simulation. This figure shows that the $N_M = 4$ and biased condition (Figure 6a) evolves towards a dispersed state while the $N_M = 4$ and randomized condition (Figure 6c) remains in a dispersed state over the course of the simulation. Conversely, the $N_M = 154$ and biased condition (Figure 6b) remains as a macrophase separated aggregate and unchanged during the span of the simulation while there is prominent coarsening in the $N_M = 154$ and randomized initial condition (Figure 6d). Figure 5 and Figure 6 demonstrate the DMFT's capability to capture non-equilibrium phase behavior. From this, we observe how the PNCs in each condition evolve.

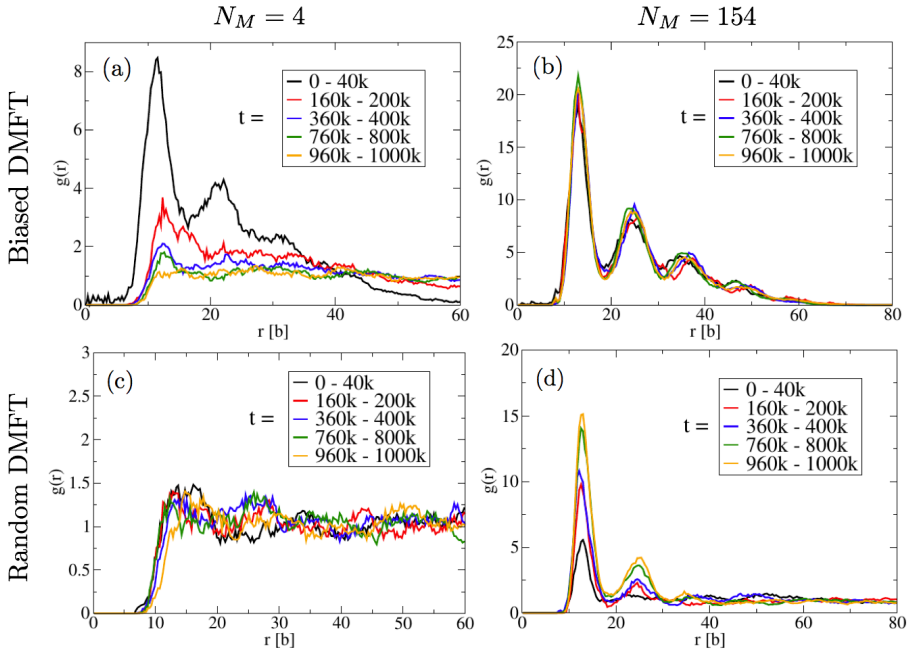

Figure 6. RDF evolution for $N_M = 4$ (a),(c) and $N_M = 154$ (b),(d) each with the nanoparticles initially biased (a),(b) and initially randomized (c),(d). Each curve represents the RDF calculated at different time windows where t = 0 to 40,000 (black), t = 160,000 to 200,000 (red), t = 360,000 to 400,000 (blue), t = 760,000 to 800,000 (green), and t = 960,000 to 1,000,000 (orange). Each condition is averaged over 3 trajectories.

To quantify the evolution of the PNCs further, we calculate the mean-squared displacement (MSD) of the nanoparticles for each matrix molecular weight condition, for both the random and biased initializations, in Figure 7. The MSD of the nanoparticles provides an assessment of how far the nanoparticles have moved over the course of the simulation. We stress that this is a qualitative comparison as the dynamics are based on a Rouse model with Flory interactions and it is unclear how the relative magnitude of the nanoparticle and polymer mobility coefficients change as the matrix molecular weight is increased. Figure 7 shows the nanoparticles move less as the matrix

molecular weight increases. This result is consistent with larger chains diffusing more slowly than shorter chains and thus, making it more difficult for the nanoparticles to move around.

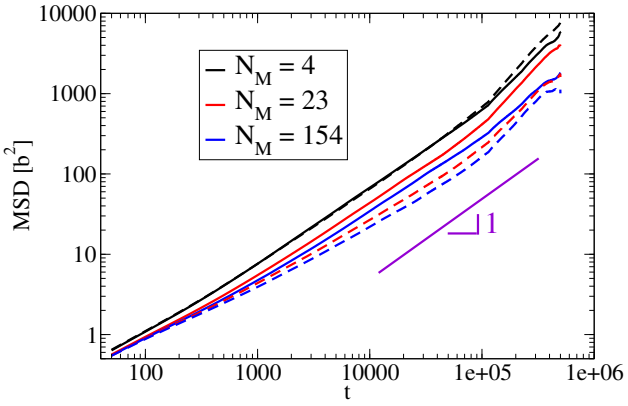

Figure 7. Mean-squared displacement (MSD) for N_M = 4 (black), N_M = 23 (red), and N_M = 154 (blue). The solid lines are the random DMFT simulations while the dashed lines are the biased DMFT simulations. The purple line denotes a reference line with a slope equal to 1. The MSD was averaged over 3 trajectories for each condition.

While Figure 7 only provides a qualitative comparison of the dynamics in the different conditions, this behavior explains why the biased N_M = 4 condition reaches its equilibrium state at t = 1,000,000 in Figure 6a while the random N_M = 154 condition is still coarsening and evolving towards its equilibrium state at t = 1,000,000 (Figure 6d). Both the random and biased N_M = 4 conditions have similar MSD curves as the simulations are evolving towards a dispersed state. However, the MSD for N_M = 23 and N_M = 154 differ depending on whether the nanoparticles are biased or randomized. Figure 7 shows that the biased nanoparticles in this regime move less. This is due to the nanoparticles being in a larger cluster and the nanoparticles on average are more confined to the movement of the single cluster compared to the randomized particles, which have single nanoparticles moving around in the box or nanoparticles that are part of smaller clusters.

An important result from these simulations demonstrate that it is more challenging for nanoparticles to reach an equilibrium macrophase separated state than an equilibrium dispersed state. Specifically, as the nanoparticles coarsen into larger clusters, the clusters move more slowly and there is a reduced likelihood of the clusters merging to form a single aggregate, though the dependence of this slowdown on the size of the aggregate will likely not be accurately captured by our simulations that neglect hydrodynamic interactions and entanglement effects. Significantly longer trajectories would be necessary to see the N_M = 154 random condition match the N_M = 154 biased

condition.

Finally, we make qualitative comparisons to experiments consisting of poly(styrene) (PS) grafted gold nanorods in a poly(methyl methacrylate) (PMMA) matrix. Figure 8 shows a side-by-side visual comparison of the experiments and the random DMFT simulations where similar phase behavior is observed. Figure 9 shows the RDF of biased DMFT simulations, random DMFT simulations, and analogous experimental systems. Interestingly, in the high matrix molecular weight condition, we observe that the initial condition of the DMFT simulations affects the comparison to the experiments. Strikingly, when the DMFT simulations are randomized, the first peak of the RDF and the RDF at relatively larger distances match near perfectly with the experiments while the biased DMFT simulations largely overshoot the RDF of the experiments at short distances and unlike the random DMFT simulations and the experiments, the RDF goes to 0 at larger distances. The discrepancy of the random DMFT simulations and the experiments at moderate distances is because we are modeling nanospheres while the experiments consist of nanorods. As a result, the nanoparticles are going to pack differently and the RDF is not a perfect one-to-one comparison. Nevertheless, Figure 8 and Figure 9b support the conclusion that the experiments are not in their equilibrium macrophase separated state but rather in a non-equilibrium or kinetically trapped state. We emphasize that the comparison of the theory to the experiments is qualitative in that we are modeling nanospheres and not nanorods and the theory contains no description of the solvent evaporation process or casting of the nanocomposite into a thin film.

VI. SUMMARY AND DISCUSSION

In this study, we conducted a direct comparison of the effectiveness of the PNC-FT and DMFT approaches in their ability to characterize grafted PNCs. Specifically, we analyzed the effect of both the uniform grafting approximation and mean-field approximation on the phase behavior of PNCs. The uniform grafting approximation becomes increasingly inaccurate as the grafting density and grafted chain length are decreased. The inclusion of thermal fluctuations affects the macro PNC phase behavior when the system is near the phase separated-dispersion phase boundary and reduces the order of packing in aggregated particles. The PNC-FT method is most efficiently used with a uniform grafting and a mean-field approximation though the DMFT method trivially circumvents these approximations. Moreover, the DMFT method gives a route to analyze kinetic pathways in the assembly of PNC systems. Often systems are not in equilibrium and understand-

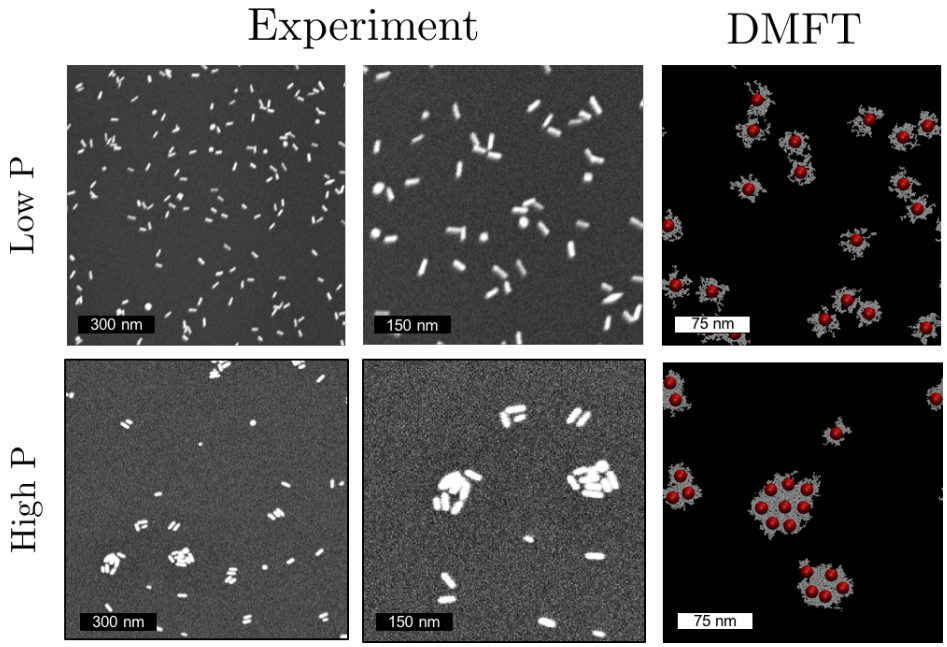

Figure 8. Experiment and random DMFT visualization. The experiments are SEM images for zoomed-out and zoomed-in images while the DMFT is a snapshot at t = 1,000,000. The DMFT snapshots are the same associated snapshots in Figure 5 but shown here to provide a more direct visual comparison to the experiments. The experiments consist of AuNRs approximately 12nm in diameter and 40nm in length and have a volume fraction of 3%. The experimental grafting density is approximately 0.28 chains/nm^2. The DMFT simulations are setup to match these parameters (see Numerical Parameters) though the nanoparticles are modeled as spheres 12nm in diameter.

ing the dynamics or non-equilibrium nature of the system can be insightful for comparisons with experiments. In this regard, the DMFT method is a more powerful tool to analyze PNC phase behavior than the PNC-FT framework, particularly if the structure is not in equilibrium or is based on particular processing conditions. In particular, comparison of DMFT simulations to experimental observations of phase behavior of polymer-grafted nanorods demonstrated that the experiments are most likely in a kinetically-trapped state. The DMFT simulations also revealed that it is more difficult for the nanoparticles to reach an equilibrium macrophase separated state than it is for them to reach an equilibrium dispersed state, due to slow coarsening kinetics of nanoparticle clusters.

Although the DMFT method trivially circumvents the mean-field and uniform grafting approximations, this should not suggest that the SCFT and CL methods are not useful. The SCFT method is extremely efficient computationally and provides a means to quickly approximate the

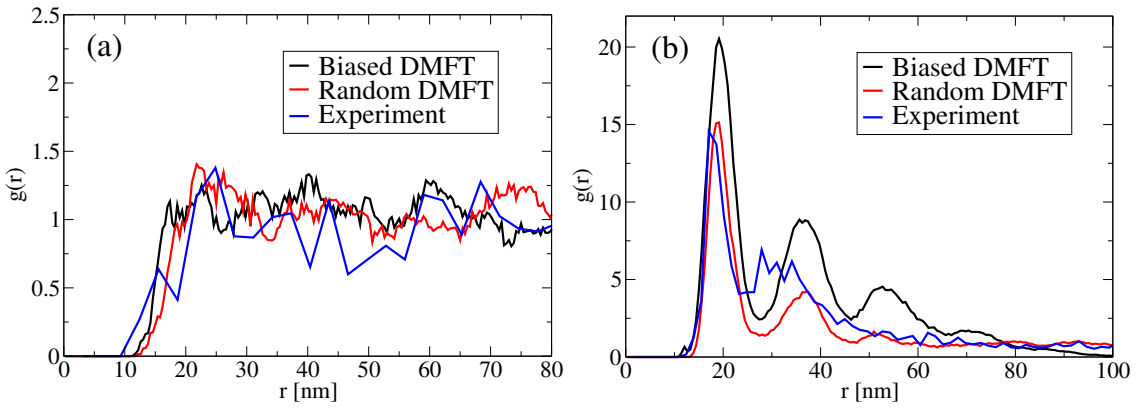

Figure 9. RDF comparison between biased DMFT simulations (black), random DMFT simulations (red), and the experiments (blue). The RDFs are calculated from t = 960,000 to 1,000,000. The theory is for N_M = 2 kg/mol (a) and N_M = 77 kg/mol (b) while the experiments are done at N_M = 1.1 kg/mol (a) and N_M = 77 kg/mol (b). The DMFT simulations are averaged over 3 trajectories.

equilibrium state of the system. The SCFT method also provides direct access to the free energy and makes assessing the global or local stability of different phases or architectures trivial. The CL framework provides the same advantages as SCFT except that while CL includes thermal fluctuations, reaching an equilibrated state requires more computational time. Furthermore, in CL accessing the free energy requires more advanced methods such as thermodynamic integration[43,64] or Bennett's method[65,66]. Furthermore, the numerical stability of CL simulations is substantially less than SCFT calculations, particularly as the dimensionless chain density C is lowered. While significant advances have been made with CL simulations, the lower limit on C that has been successfully simulated is approximately 3[43]. Unlike CL, the DMFT method is able to model low C values with seemingly no stability issues.

The SCFT, CL, and DMFT models are also written in a formalism that is easily mapped to experiments through simply needing to map the statistical segment length of the polymer and the Flory χ parameter. Furthermore, all three of these methods provide a clear advantage in describing macro phase behavior of PNCs over atomistic or even bead-spring coarse-grained models of PNCs from a computational standpoint. Specifically, accessing a large nanoparticle phase space in particle simulations can be challenging because nanoparticle diffusion is severely hindered, particularly in entangled polymer systems. Additionally, it is difficult to assess when the system is in an equilibrium or non-equilibrium state. While the DMFT framework shares the difficulty of assessing whether the system is in a non-equilibrium or equilibrium state, we see that unlike atom-

istic and bead-spring coarse-grained simulations, with DMFT we can explore a large PNC phase space, easily access a diffusive regime, and improve the confidence that we are in a stable regime.

ACKNOWLEDGMENTS

This work was performed, in part, at the Center for Integrated Nanotechnologies, an Office of Science User Facility operated for the U.S. Department of Energy (DOE) Office of Science (J.P.K., A.L.F.). Sandia National Laboratories is a multi-mission laboratory managed and operated by National Technology and Engineering Solutions of Sandia, LLC., a wholly owned subsidiary of Honeywell International, Inc., for the U.S. Department of Energy's National Nuclear Security Administration under contract DE-NA-0003525. Support was also provided by the NSF/MRSEC-DMR 11-20901 (R.J.C.), NSF DMR-1410246 (J.P.K., R.A.R.), Polymer Programs DMR15-07713 (R.J.C.) as well as ACS/PRF 54028-ND7 (R.J.C).

REFERENCES

[1]S. Kango, S. Kalia, A. Celli, J. Njuguna, Y. Habibi, and R. Kumar, Progress in Polymer Science **38**, 1232 (2013).

[2]M. J. A. Hore and R. J. Composto, ACS Nano **4**, 6941 (2010).

[3]M. J. A. Hore and R. J. Composto, Macromolecules **45**, 6078 (2012).

[4]M. J. A. Hore and R. J. Composto, Macromolecules **47**, 875 (2014).

[5]R. C. Ferrier Jr, H.-S. Lee, M. J. A. Hore, M. Caporizzo, D. M. Eckmann, and R. J. Composto, Langmuir **30**, 1906 (2014).

[6]P. F. Green, Soft Matter **7**, 7914 (2011).

[7]S. Srivastava, P. Agarwal, and L. A. Archer, Langmuir **28**, 6276 (2012).

[8]D. Sunday, J. Ilavsky, and D. L. Green, Macromolecules **45**, 4007 (2012).

[9]S. K. Kumar, N. Jouault, B. Benicewicz, and T. Neely, Macromolecules **46**, 3199 (2013).

[10]P. Akcora, H. Liu, S. K. Kumar, J. Moll, Y. Li, B. C. Benicewicz, L. S. Schadler, D. Acehan, A. Z. Panagiotopoulos, V. Pryamitsyn, V. Ganesan, J. Ilavsky, P. Thiyagarajan, R. H. Colby, and J. F. Douglas, Nature Materials **8**, 354 (2009).

[11]C.-C. Lin, E. Parrish, and R. J. Composto, Macromolecules **49**, 5755 (2016).

[12]S. K. Kumar, B. C. Benicewicz, R. A. Vaia, and K. I. Winey, Macromolecules **50**, 714 (2017).

[13]A. Bansal, H. Yang, C. Li, K. Cho, B. C. Benicewicz, S. K. Kumar, and L. S. Schadler, Nature Materials **4**, 693 (2005).

[14]M. J. A. Hore, A. L. Frischknecht, and R. J. Composto, ACS Macro Letters **1**, 115 (2012).

[15]N. Jouault, D. Lee, D. Zhao, and S. K. Kumar, Advanced Materials **26**, 4031 (2014).

[16]P. W. Majewski, M. Gopinadhan, and C. O. Osuji, Journal of Polymer Science Part B: Polymer Physics **50**, 2 (2012).

[17]V. Raman, A. Bose, B. D. Olsen, and T. A. Hatton, Macromolecules **45**, 9373 (2012).

[18]J. Kao, K. Thorkelsson, P. Bai, B. J. Rancatore, and T. Xu, Chemical Society Reviews **42**, 2654 (2013).

[19]K. Wang, S. Liang, R. Du, Q. Zhang, and Q. Fu, Polymer **45**, 7953 (2004).

[20]Y. Liu, E. N. Mills, and R. J. Composto, Journal of Materials Chemistry **19**, 2704 (2009).

[21]K. M. Ryan, A. Mastroianni, K. A. Stancil, H. Liu, and A. Alivisatos, Nano Letters **6**, 1479 (2006).

[22]S. Gupta, Q. Zhang, T. Emrick, and T. P. Russell, Nano Letters **6**, 2066 (2006).

[23]W. Ahmed, E. S. Kooij, A. Van Silfhout, and B. Poelsema, Nano Letters **9**, 3786 (2009).

[24]J. B. Hooper and K. S. Schweizer, Macromolecules **39**, 5133 (2006).

[25]L. M. Hall and K. S. Schweizer, J. Chem. Phys. **128** (2008), 10.1063/1.2938379.

[26]A. Jayaraman and K. S. Schweizer, Macromolecules **42**, 8423 (2009).

[27]L. M. Hall, A. Jayaraman, and K. S. Schweizer, Current Opinion in Solid State and Materials Science **14**, 38 (2010).

[28]T. B. Martin, P. M. Dodd, and A. Jayaraman, Physical Review Letters **110**, 018301 (2013).

[29]R. B. Thompson, V. V. Ginzburg, M. W. Matsen, and A. C. Balazs, Science **292**, 2469 (2001).

[30]R. B. Thompson, V. V. Ginzburg, M. W. Matsen, and A. C. Balazs, Macromolecules **35**, 1060 (2002).

[31]R. B. Thompson, K. O. Rasmussen, and T. Lookman, The Journal of Chemical Physics **120**, 31 (2004).

[32]M. Matsen and R. Thompson, Macromolecules **41**, 1853 (2008).

[33]A. L. Frischknecht, M. J. A. Hore, J. Ford, and R. J. Composto, Macromolecules **46**, 2856 (2013).

[34]T. Zhang, C. Fu, Y. Yang, and F. Qiu, The Journal of Chemical Physics **146**, 054902 (2017).

[35]V. Ganesan and A. Jayaraman, Soft Matter **10**, 13 (2014).

[36]S. K. Kumar, V. Ganesan, and R. A. Riggleman, The Journal of Chemical Physics **147**, 020901 (2017).

[37]J. Koski, H. Chao, and R. A. Riggleman, The Journal of Chemical Physics **139**, 244911 (2013).

[38]H. Chao, B. A. Hagberg, and R. A. Riggleman, Soft Matter **10**, 8083 (2014).

[39]J. Koski, H. Chao, and R. A. Riggleman, Chemical Communications **51**, 5440 (2015).

[40]G. H. Fredrickson and H. Orland, The Journal of Chemical Physics **140**, 084902 (2014).

[41]H. Chao, J. Koski, and R. Riggleman, Soft Matter **13**, 239 (2016).

[42]S. W. Sides, B. J. Kim, E. J. Kramer, and G. H. Fredrickson, Physical Review Letters **96**, 250601 (2006).

[43]K. T. Delaney and G. H. Fredrickson, The Journal of Physical Chemistry B **120**, 7615 (2016).

[44]V. Ganesan and V. Pryamitsyn, The Journal of Chemical Physics **118**, 4345 (2003).

[45]K. C. Daoulas and M. Müller, The Journal of Chemical Physics **125**, 184904 (2006).

[46]D. Q. Pike, F. A. Detcheverry, M. Müller, and J. J. de Pablo, J. Chem. Phys. **131**, 84903 (2009).

[47]A. E. Likhtman, Macromolecules **38**, 6128 (2005).

[48]A. Ramírez-Hernández, F. A. Detcheverry, B. L. Peters, V. C. Chappa, K. S. Schweizer, M. Mller, and J. J. de Pablo, Macromolecules **46**, 6287 (2013).

[49]A. Ramírez-Hernández, M. Müller, and J. J. De Pablo, Soft Matter **9**, 2030 (2013).

[50]A. Nikoubashman, R. L. Davis, B. T. Michal, P. M. Chaikin, R. A. Register, and A. Z. Panagiotopoulos, ACS Nano **8**, 8015 (2014).

[51]J. D. Schieber and M. Andreev, Annual Review of Chemical and Biomolecular Engineering **5**, 367 (2014).

[52]B. Nikoobakht and M. A. El-Sayed, Chemistry of Materials **15**, 1957 (2003).

[53]T. K. Sau and C. J. Murphy, Langmuir **20**, 6414 (2004).

[54]E. Helfand, The Journal of Chemical Physics **62**, 999 (1975).

[55]G. H. Fredrickson, *The Equilibrium Theory of Inhomogeneous Polymers* (Oxford University Press, New York, 2006).

[56]P. M. Chaikin and T. C. Lubensky, *Principles of Condensed Matter Physics*, Vol. 1 (Cambridge Univ Press, 2000).

[57]M. C. Villet and G. H. Fredrickson, The Journal of Chemical Physics **141**, 224115 (2014).

[58]E. M. Lennon, G. O. Mohler, H. D. Ceniceros, C. J. García-Cervera, and G. H. Fredrickson, Multiscale Modeling and Simulation **6**, 1347 (2008).

[59]N. Grønbech-Jensen and O. Farago, Molecular Physics **111**, 983 (2013).

[60]M. Deserno and C. Holm, The Journal of Chemical Physics **109**, 7678 (1998).

[61]R. W. Hockney and J. W. Eastwood, *Computer Simulation Using Particles* (CRC Press, 1988).

[62]R. C. Ferrier Jr, J. Koski, R. A. Riggleman, and R. J. Composto, Macromolecules **49**, 1002 (2016).

[63]O. K. C. Tsui, *Polymer Thin Films*, Vol. 1 (World Scientific, 2008).

[64]E. Lennon, K. Katsov, and G. H. Fredrickson, Physical Review Letters **101**, 138302 (2008).

[65]R. A. Riggleman, R. Kumar, and G. H. Fredrickson, J. Chem. Phys. **136**, 24903 (2012).

[66]J. P. Koski and R. A. Riggleman, The Journal of Chemical Physics **146**, 164903 (2017).